Accepted Manuscript

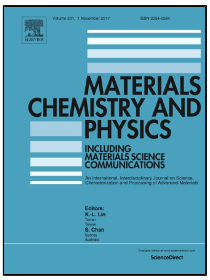

Thickness dependence of the superconducting properties of γ- Mo_2N thin films on Si (001) grown by DC sputtering at room temperature

N. Haberkorn, S. Bengio, H. Troiani, S. Suárez, P.D. Pérez, P. Granell, F. Golmar, M. Sirena, J. Guimpel

PII:	S0254-0584(17)30797-6
DOI:	10.1016/j.matchemphys.2017.10.015
Reference:	MAC 20054
To appear in:	*Materials Chemistry and Physics*
Received Date:	07 January 2017
Revised Date:	18 August 2017
Accepted Date:	07 October 2017

Please cite this article as: N. Haberkorn, S. Bengio, H. Troiani, S. Suárez, P.D. Pérez, P. Granell, F. Golmar, M. Sirena, J. Guimpel, Thickness dependence of the superconducting properties of γ- Mo_2N thin films on Si (001) grown by DC sputtering at room temperature, *Materials Chemistry and Physics* (2017), doi: 10.1016/j.matchemphys.2017.10.015

- Superconducting Mo-N thin films were grown at room temperature by reactive DC sputtering.
- The films display γ-Mo_2N structure with nanometric grains.
- Thick films display a superconducting transition temperature around 6.6 K.
- Superconductivity close 3 K is preserved for 5 nm thick films.

Thickness dependence of the superconducting properties of γ- Mo_2N thin films on Si (001) grown by DC sputtering at room temperature

N. Haberkorn,[1,2] S. Bengio,[1] H. Troiani,[1,2] S. Suárez,[1,2] P. D. Pérez,[1] P. Granell,[3] F. Golmar,[3,4] M. Sirena,[1,2] J. Guimpel.[1,2]

[1] *Consejo Nacional de Investigaciones Científicas y Técnicas, Centro Atómico Bariloche, Av. Bustillo 9500, 8400 San Carlos de Bariloche, Argentina*.

[2] *Instituto Balseiro, Universidad Nacional de Cuyo, Av. Bustillo 9500, 8400 San Carlos de Bariloche, Argentina*

[3] *INTI-CMNB, Av. Gral Paz 5445 (B1650KNA), San Martín, Buenos Aires, Argentina*.

[4] *Consejo Nacional de Investigaciones Científicas y Técnicas, Escuela de Ciencia y Tecnología, UNSAM, Campus Miguelete, (1650), San Martín, Buenos Aires, Argentina.*

Abstract

We study the crystalline structure and superconducting properties of γ-Mo_2N thin films grown by reactive DC sputtering on AlN buffered Si (001) substrates. The films were grown at room temperature. The microstructure of the films, which was studied by X-ray diffraction and transmission electron microscopy, shows a single-phase with nanometric grains textured along the (200) direction. The films exhibit highly uniform thickness in areas larger than 20 x 20 μm^2. The superconducting critical temperature T_c is suppressed from 6.6 K to ≈ 3.0 K when the thickness decreases from 40 nm to 5 nm. The residual-resistivity ratio is slightly smaller than 1 for all the films, which indicates very short electronic mean free path. The films are in the superconducting dirty limit with upper critical field H_{c2} (0) ≈ 12 T for films with thickness of 40 nm, and 9 T for films with thickness of 10 nm. In addition, from the critical current densities J_c in the vortex-free state, we estimate a penetration depth λ(0) ≈ (800 ± 50) nm and a thermodynamic critical field H_c (0) = (500 ± 80 Oe).

e-mail corresponding author: *nhaberk@cab.cnea.gov.ar* Tel : +54 0294 444 5147- FAX: +54 0294 444 5299

Keywords: thin films, superconductivity,

1. *Introduction*

Transition–metal nitrides (TMN) display a wide range of electronic and mechanical properties which are promising for technological applications. Devices based in superconducting thin films include tunnel junctions [1], hot electron bolometers [2], single photon detectors [3], etc. The molybdenum nitrides possess several crystalline phases: γ-Mo_2N (cubic) with superconducting transition temperature $T_c \sim 5$ K [4], β-Mo_2N (tetragonal) with $T_c \sim 5$ K [5] and δ-MoN (hexagonal) with $T_c \sim 12$ K. [6,7]. The synthesis of bulk γ-Mo_2N and δ-MoN usually requires high-pressure and high-temperature [7,8,9]. The extreme conditions usually applied for the synthesis of bulk specimens can be avoided by growing thin films. Molybdenum nitride thin films have been grown by several techniques such as reactive sputtering [10], pulsed laser deposition (PLD) [11], thermal nitration [12] and chemical methods [13]. The properties of the MoN_x films strongly depend on the actual growth conditions, and consequently on the processing parameters [10,14]. The microstructure of the films is directly related to the resulting superconducting properties. A superconductor with very few structural (crystalline and impurities) defects and electronic mean free path (l) much larger than the intrinsic coherence length ξ_0 is in the "clean limit". If disorder increases then l decreases, and the superconductor reaches the "dirty limit when $l / \xi_0 < 1$". Increasing disorder reduces the effective ξ and enlarges the penetration depth λ, thus increasing $\kappa = \lambda / \xi$, while maintaining the product $\xi\lambda$ constant to first approximation [15].

Most of the technological applications based in superconducting TMN thin films require uniform electronic properties on large areas [16,17,18]. In addition, some devices such as single photon detectors require uniform superconducting properties in paths printed in very thin films [19]. Recently, the synthesis of superconducting γ-Mo_2N thin films in the dirty limit has been reported [20]. The particularity is that the films were grown on oxidized silicon wafers as substrates at room temperature**.** The simplicity in the growth process of γ-Mo_2N thin films is promising for low temperature superconducting devices. For that, the thickness dependence on the superconducting properties is of fundamental technological relevance [3].

In this work we analyze the superconducting properties of γ-Mo_2N thin films grown by reactive DC sputtering on AlN buffered Si (001) substrates. The objective of this work is to analyze the crystalline structure and superconducting properties of γ-Mo_2N thin films grown at room temperature. This is important considering the potential technological application in devices such as single photon detectors. Thin films with thickness between 5 nm and 260 nm were grown. For film thicker than 40 nm, the superconducting transition temperature (T_c) was found to be independent of the film thickness. All the studied films are in the thickness limit $d << \lambda$. The films are single phase γ-Mo_2N with nanometric grains textured along the <200> direction. The thickness is highly constant on areas larger than 20 x 20 μm^2. The temperature dependence of the upper critical fields H_{c2} were determined for films with thickness between 5 nm and 40 nm. The films are in the superconducting dirty limit. For magnetic field perpendicular to the surface, the films display upper critical fields H_{c2} close to the prediction for the Pauli limit $H_p \approx 1.84\ T_c$. In addition, for films thinner than 20 nm, we

identify the vortex-free state for magnetic fields applied parallel to the surface. In this configuration and from the temperature dependence of the critical current density J_c (T) close to T_c, we estimate the depairing critical current J_0, the thermodynamic critical field H_c and the penetration depth λ.

2. *Material and methods*

γ-Mo_2N films were deposited on AlN buffered Si (001) substrates by reactive DC magnetron sputtering without any intentional heating of the substrate. The AlN buffer layer was introduced to avoid any chemical reaction between the Mo and the SiO_2 top layer of the Si wafers, which could be relevant in very thin films. It is important to mention that chemical reaction between Mo and SiO_2 (dead superconducting layer) can also be avoided (without using a buffer layer) removing the native SiO_2 layer by chemical etching with hydrofluoridric acid [21]. In that case the superconducting properties of very thin films should be similar to that obtained in our work. The AlN buffer layer was selected considering the chemical compatibility with superconducting metal nitrides [22]. Since films grown at room temperature are polycrystalline [20], structural matching at the interfaces is not expected. The residual pressure of the chamber was less than 10^{-6} Torr. Ultra-high purity Ar (99.999%) and N_2 (99.999%) were used as gas sources. The substrates were not heated during the deposition of the films. Commercial sputtering targets of Al (diameter: 38 mm) and Mo (diameter: 38 mm) were used. The AlN and Mo_2N layers were grown by reactive RF and DC magnetron sputtering, respectively. During deposition the target to substrate distance was ~ 7 cm. The target power was 100 W (AlN) and 50 W (Mo_2N) and the total pressure at the chamber was 5 mTorr (80:20, Ar: N_2). The films were grown in 1 cm x 1 cm square Si (001) substrates. The film thickness was calibrated by low-angle x-ray reflectivity. The AlN growth rate was 8 nm / min. The Mo growth rate was 20 nm / min. Although the results are not included, the increment in the target power from 50 W to 100 W for Mo_2N increases the growth rate from 20 nm / min to ≈ 52 nm / min without appreciable changes in the superconducting properties of the films. The results presented in this work correspond to films grown at 50 W.

The microstructure of the films was analyzed by X-ray diffraction (XRD) and transmission electron microscopy (TEM). XRD data were obtained using a Panalytical Empyrean equipment. TEM results were obtained using a TEM CM200 UT microscope operated at 200kV. For TEM analysis, a thin lamella was prepared with a Gallium focused ion beam (FEI Helios Nanolab 650). The lamella was polished with ion beam energies of 5kV and 2kV in order to minimize Ga damage to the sample. The chemical stoichiometry of the films was analyzed by Rutherford Backscattering Spectroscopy (RBS) with a TANDEM (NEC, 1.7 MV) accelerator using a 2 MeV $4He^{2+}$ ion beam. Surface composition was investigated by means of X-ray photoelectron spectroscopy (XPS) using a standard Al/Mg twin-anode, X-ray gun and a hemispherical electrostatic electron energy analyzer. The samples were measured in high-vacuum conditions with a base pressure of 10^{-9} Torr. The Fermi level and/or adventitious Carbon was used as reference to calibrate the binding-energy (BE) scale. The topology of the films was characterized by atomic force microscopy (AFM)

measurements in a Dimension 3100©Brucker microscope. A detailed morphological characterization of the films was made by analyzing the topographic information at different scale lengths (1 μm and 20 μm). The AFM images were obtained in tapping mode. The electrical transport measurements were performed on 1 mm (length) x 0.04 mm (width) bridges. A standard four-terminal transport technique was used to measure I–V curves.

3. Results and discussion

3a. Structural and chemical composition analysis of the films

The surface roughnesses for films with different thickness were analyzed by AFM. The films display extremely flat surfaces with root mean squared (RMS) roughness below 0.5 nm even for films thicker than 100 nm. In addition, 5 nm thick films grow homogenously with rms of 0.3 nm (see Figs. 1*a* and 1*b*). The thickness homogeneity of the films in 1 square centimeter was verified by low angle XRD. The measurements were performed in different pieces (0.15 cm x 0. 3 cm) of a 80 nm thick Mo_2N thin film grown without an AlN buffer layer (see Fig. 1*c*). Profile fitting was done using the Parratt32 code [23]. According with the fitting the variations between the piece 1 (center, $d = (78.2 \pm 0.2)$ nm) and piece 3 (border, $d = (78.7 \pm 0.2)$ nm) are ≈ 0.5 nm, which represents a thickness variation < 1 %. The chemical composition of the films was verified by RBS being $Mo_2N_{1.1\pm0.1}$, which is within expectations for cubic γ-Mo_2N. Figure 2a shows an XRD pattern obtained in a 260 nm thick $Mo_2N_{1.1\pm0.1}$ film. The peak corresponds to the (200) reflection of the cubic γ-Mo_2N with lattice parameter $a = (0.4213 \pm 0.0002)$ nm. Figs. 2*b*-*c* show XRD pole figures for the (200), (220) and (111) reflection corresponding to the cubic γ-Mo_2N. The pole figures indicate that the film is polycrystalline and textured along the (200) reflection with a rocking curve width of ≈ 11.5°. The microstructure of the films was analyzed for a 40 nm thick γ-Mo_2N grown on 8 nm AlN / Si (100). Figure 3*a* shows a TEM image where the uniformity in the film thickness of both γ-Mo_2N and AlN buffer layer are identified. Figure 3*b* shows a high resolution TEM image of the γ-Mo_2N. A columnar grain with diameter smaller than 10 nm can be identified from Fourier filtered image (Fig. 3*c*) using the 111 spots indicated in the inset of Fig. 3*b*.

X Ray Photoelectron Spectroscopy (XPS) measurements were performed to obtain information of the film surface chemical composition and the oxidation state of the Mo. The photoelectron peaks Mo3d, O1s, C1s and N1s were measured in detail, being the N1s overlapped with the Mo3p peak. The surface cleaning was performed with Ar^+ sputtering (2kV), after which the C1s peak disappeared while the O1s peak still remained. Long survey XPS spectrum for the cleaned surface in a 260 nm thick Mo_2N film is shown in Fig 4*a*. The Mo3d binding energy region for the pristine and clean surface is shown in Figs. 4*b* and 4*c*, respectively. Each of these elemental spectra is composed of two identical peaks that correspond to the spin orbit split $3d_{5/2}$ and

$3d_{3/2}$ for the Mo, with relative intensities of 3:2. The spectra were fitted using a Voight function for each peak plus a Shirley-type background. The total fitted intensities along with the experimental ones are shown in each spectrum. We identified up to three components in the Mo3d spectra, a major component at binding energy 228.6 eV, a minor component at 230 eV and a remaining component in the higher binding energy region at 232.7 eV. The major component can be ascribed to $Mo^{\delta+}$ ($2 \leq \delta < 4$), the minor component to Mo^{4+} and the remaining component to Mo^{6+} oxidation state [24].This last component at binding energy 232.7 eV disappears after cleaning the surface and can be associated with the formation of surface MoO_3 [25].The major component at binding energy 228.6 eV was previously associated with the compound Mo_2N and attributed to $Mo^{\delta+}$ ($2 \leq \delta < 4$) [25,26]. The minor component at binding energy ≈ 230 eV can be associated with Mo^{4+} [26,27] and it could be related to MoO_2 impurities. This fact is in agreement with the presence of oxygen even for cleaned surfaces, as we mentioned above. It is important to note that the XPS spectra for the γ-Mo_2N phase is weakly affected by small changes in chemical composition [28]. Since no crystalline structure changes are observed as a function of film thickness, no changes are expected in the XPS spectra.

3b. Electrical transport

Figure 5 shows the thickness-dependence of the T_c for films with thickness of 5 nm, 10 nm, 15 nm, 20 nm, 40 nm. Wherever used, the notation *d*X indicates a Mo_2N films with thickness X in nm. The independence of T_c with thickness, for films thicker than 40 nm, was verified for *d*57 and *d*570. The inset in Fig. 5 shows the temperature dependence of the resistivity at $T < 10$ K for the measured films. The superconducting transition is sharp independently of the thickness. For films thicker than 5 nm, the transition width is ≤ 0.1 K. A slight broadening of the superconducting transition is observed for *d*5. This can be attributed to enhanced thermal fluctuations in two dimensions when the sample thickness falls below the bulk out-of-plane ξ≈ 6 nm [15]. The T_c of films with $d > 40$ nm is 6.6 K, which is slightly higher than the value reported for epitaxial γ- Mo_2N films [29] and is slightly smaller than that reported in ref. [20]. For films thinner than 40 nm the T_c is systematically suppressed and $T_c = 3$ K is observed for *d*5 (see Table 1). The resistivity of the films depends only very weakly on temperature in the range $10 < T < 300$ K. The residual resistance ratio (*RRR*) defined as *R* (300 K) / *R*(10 K) where *R* is the sample resistance, is slightly smaller than one (≈ 0.90-0.93) for all the studied films [20]. The resistivity of the films is independent of the thickness $\rho^{(300\ K)} = 2.8 \times 10^{-4}$ -3.2 $\times 10^{-4}$ Ω.cm. This fact indicates a very short $l < 5$ nm due to small grains, chemical impurities or vacancies and structural defects.

Figures 6*a-d* show H_{c2} ($t = T/T_c$) for the *d*5, *d*10, *d*15 and *d*40. The $H_{c2}(t)$ values were measured with the magnetic field parallel ($H_{c2}^{\parallel}$) and perpendicular ($H_{c2}^{\perp}$) to the surface. It is important to mention that, since Mo_2N displays a cubic structure, crystalline anisotropy is not expected. The differences in $H_{c2}^{\parallel}$ and $H_{c2}^{\perp}$ should be related to dimensional effects [15]. For the perpendicular field case, films with $d > 10$ nm display

$H_{c2}^{\perp}$ ($t \rightarrow 0$) above 9 T. These values are comparable to those obtained in epitaxial δ-MoN thin films obtained by chemical methods [30]. The temperature dependence of $H_{c2}^{\perp}$ can be analyzed by the Werthamer-Helfand-Hohenberg (WHH) model developed for dirty one band superconductors [31], which is described below. For the parallel field case, films thinner than 20 nm show a dependence $H_{c2}^{\parallel}(T) \propto (1-t)^{1/2}$, expected for 2*D* behavior [32]. For *d*40, the 2*D* behavior is expected only for $T \rightarrow T_c$. The 2*D* to 3*D* crossover temperature is dependent on the thickness, and it is expected to appear when the ratio $d/\xi(T) = 4.4$ [33].

The temperature-dependence of $H_{c2}^{\perp}$ determined by the orbital and spin-paramagnetic effect in one band, and for dirty superconductors is given by the Werthamer-Helfand-Hohenberg (WHH) formula

$$ln\frac{1}{t} = \sum_{v=-\infty}^{\infty}\left(\frac{1}{|2v+1|} - \left[|2v+1| + \frac{\hbar}{t} + \frac{(\alpha\hbar/t)^2}{|2v+1| + (\hbar+\lambda_{so})/t}\right]^{-1}\right) \text{ [eq. 1]}$$

where $t = T / T_c$, $\hbar = (4/\pi^2)\left(H_{c2}(T)/\left|dH_{c2}/dT\right|_{T_c}\right)$, α is the Maki parameter, and λ_{so} is the spin-orbit scattering constant. When $\lambda_{so} = 0$, $H_{c2}(0)$ obtained from the WHH formula satisfies the relation

$$H_{c2}(0) = \frac{H_{c2}^{orb}(0)}{\sqrt{1+\alpha^2}} \text{ [eq. 2]}$$

which was originally derived by K. Maki [34]. In Fig. 6, we note that the $H_{c2}(t)$ curve for *d*40 satisfies the prediction of the WHH model considering $\alpha = 0$ and $\lambda_{so} = 0$. For *d*10 and *d*15 (with suppressed T_c) , the $H_{c2}(t)$ dependences cannot be adjusted with $\alpha = 0$ and $\lambda_{so} = 0$. For this case, using $\alpha = 0.8$ -1 and $\lambda_{so} = 0$, the $H_{c2}(t)$ dependences are well described. The Maki parameter α, quantifies the weakening influence of the Pauli electron spin paramagnetism on the superconducting state. For $\alpha = 0$ this does not play any role and $H_{c2}(t)$ is given as the pure "orbital field limit" $H_{orb}(t)$ due to the supercurrents circulating around the vortex cores. For $\alpha > 0$, the weakening of the superconducting state reduces the maximum magnetic field that the superconductor can tolerate below this orbital limit. In addition, the $H_{c2}^{\parallel}$ values for the different films are close to the Pauli paramagnetic limit $H_p \approx 1.84\ T_c$ (in Tesla for T_c in Kelvin) for isotropic BCS superconductors [35]. Above this field, it is expected that the Zeeman splitting energy matches the superconducting energy gap or binding energy of a Cooper pair. For example, H_p values of approximately 12 T and 5.5 T are expected for *d*40 and *d*5, respectively (see dashed lines in Fig. 6).

Table 1 summarizes the superconducting parameters used to fit the $H_{c2}^{\perp}(t)$ data. The ξ (0) values were estimated using $\xi(0) = \sqrt{\Phi_0/(2\pi H_{c2}^{\parallel}(0))}$ (with Φ_0 = 2.07 x 10^{-7} G cm^2 is the flux quantum). It is important to mention that larger H_{c2} values were reported in ref. [20] for non-textured films with nanometric grains, which indicates that dirtiest films (shorter mean free path *l*) can be obtained increasing the disorder.

The temperature dependence of $H_{c2}^{||}$ in the thin films can be analyzed for the 2D and 3D limits. In the 2D limit or vortex-free state is given by [15]

$$H_{c2}^{||}(T) = \frac{\sqrt{3}\Phi_0}{\pi d\xi(T)} = \frac{\sqrt{3}\Phi_0}{\pi d\left[0.855(\xi_0 l)^{1/2}\right]}(1-t)^{1/2} \quad \text{[eq. 3]}$$

The second equality arises from the Ginzburg – Landau (GL) relation in the dirty limit $\xi(T) = 0.855\xi(0)\,(1\text{-}t)^{-1/2}$. Although in principle the predicted GL temperature dependences are only valid near T_c, they usually are valid over a much wider temperature range. In the 3D limit and for flat surfaces, a cusp-like behavior in the experimental angular dependence of H_{c2} is expected when the field is close to being parallel to the surface and it can be associated with surface superconductivity [24]. The surface superconductivity produces a field enhancement of $H_{c3} = 1.69\ H_{c2}$ [24] for $H_{c2}^{||}$. This is in agreement with the enhancement observed in $H_{c2}^{||}$ in *d*40 (see Fig. 6*d*). Experimental values smaller than the theoretical prediction (dot line) can be attributed to a slight misalignment (< 0.1°) between the film and the magnetic field. On the other hand, films thinner than 20 nm should be analyzed in the 2D limit. Good agreement between the theoretical prediction (eq. 3) and experimental values are observed for *d*10 and *d*15 in Figs. 6*b*-*c*. For *d*5, a $\xi_0 = 8$ nm corresponding to $H_{c2} = H_p \approx 1.84\ T_c$ was used for the fit. In that case good agreement between the values predicted by eq. 3 and experimental data values is observed only close to T_c.

We now turn our attention to the effects on the critical current density J_c, starting with the angular dependence of J_c. Possible influence of crystalline defects on the pinning properties can be obtained from the angular J_c (Θ) measurements. Figure 7*a* shows J_c (Θ) at $\mu_0 H = 0.01$ T for *d*10 and *d*15 at 3.25 K and 3.75 K, respectively. Both temperatures corresponding to $t = T/T_c \approx 0.65$. Both samples display similar behavior. A minimum in J_c for H ⊥ S and a maximum in J_c for **H** // S. The minimum in J_c for H ⊥ S is expected from vortex pinning produced from random disorder [36], which indicates negligible pinning from the columnar growth usually observed in sputtered films at low temperatures. The maximum in J_c for **H** // S take place due to a vortex-free state and $J_c \approx$ the depairing critical current $J_0 = cH_c/3\sqrt{6\pi\lambda}$ (with *c* the light speed and H_c the thermodynamic critical field). The J_c at low fields for **H** ⊥ S represents merely ≈ 0.15 % J_0, which indicates weak vortex pinning. The very low J_c values with **H** ⊥ S can be associated with large vortex fluctuations, which can be related to the large λ expected from films in the dirty limit. In addition, the extremely smooth surfaces reduces the vortex pinning expected for boundaries between grains or islands. In very thin films, usually the roughness produced by boundaries between islands increase the pinning considerably, and values close to J_0 can be observed [37]. We analyze the J_c (T) dependence with **H** // S. In very thin films or wires and when the ratio $d/\xi(T) < 4.4$ [33], the experimental J_c should be the maximum possible critical current density limited by depairing [15,38,39]. For conventional superconductors the temperature dependence of J_0 near T_c is given by the G-L expression

$$J_0^{GL}(t) = \frac{cH_c(T)}{3\sqrt{6}\pi\lambda(T)} \propto J_0^{GL}(0)(1-t)^{3/2} \qquad \text{[eq. 4]}$$

where $H_c(0) = \frac{\Phi_0}{2\sqrt{2}\pi\lambda(0)\xi(0)}$ is the thermodynamic critical field, $H_c(t) = 1.73H_c(0)(1-t)$, $\lambda(t)|_{t\to 1} = \frac{\lambda(0)}{[2(1-t)]^{1/2}}$, and $J_0^{GL}(0)$ is the depairing current density at zero temperature, and H_c is the thermodynamic critical field [15]. For dirty superconductors $\lambda_{eff}^2 \approx \lambda_L^2\left(\frac{\xi_0}{l}\right)$. The analysis of the eq. 4 is valid if the current is uniform in the film. Figure 7*b* shows $[0.26J_0(t)/J_0(0)]^{2/3}$ versus *t* for *d*10 and *d*15 nm with **H**$_{\|}$ S (0.01 T). The expected linear dependence predicted by the eq. 4 close T_c ($t\to1$) is observed. A small the magnetic field was applied in order to avoid the presence of vortices by decreasing the transverse magnetic field component from self-field effects [30]. The *constant* 0.26 appears by considering the equivalence in the eq. 4, and the H_c (*t*) and λ (*t*) dependences. The obtained J_0 (T= 0) values are (2.7 ± 0.4) MA cm^{-2} and ≈ (2.6 ± 0.4) MA cm^{-2} for *d*10 *and d*15 *nm*, respectively. Although these values can be affected by fluctuations in the superconducting section, using eq. 4 and the relation $H_c = \frac{\Phi_0}{2\sqrt{2}\pi\lambda(0)\xi(0)}$, and ξ(0) = (6.0 ± 0.2 nm), we obtain λ(0) ≈ (800 ± 50) nm and H_c(0) = (500 ± 80) Oe. The H_c (0) value in very thin films has technological relevance for superconducting ratio frequency cavities [18]. Considering negligible vortex dissipation, deviations of λ (0) in very thin films compared to the bulk behavior may be associated to dimensional effects. In addition, inhomogeneities in the current distribution at small thickness are expected to reduce the critical currents densities. At low thicknesses, there are two effects that increase λ above the bulk value. First, for thickness < λ the effective penetration depth λ_{eff} increases and can become significantly higher than λ(0). Second, the suppression of the order parameter as measured by the decrease of T_c/T_c^{bulk}, which results in a higher value for λ(0) [15].

4. ***Conclusions***

Single phase polycrystalline γ- Mo_2N films were fabricated by DC sputtering on AlN buffered Si (001) substrates. The films display very smooth surfaces on areas above 20 x 20 μm^2, which correspond to the typical size used for tunnel junctions and radiation detectors [3,22]. Thick films display a T_c ≈ 6.6 K that is gradually suppressed for films thinner than 20 nm. A T_c ≈ 3 K was observed for a 5 nm thick film. The $H_{c2}^{\perp}$ (*t*) dependences are well described by the Werthamer-Helfand-Hohenberg (WHH) model for dirty superconductors. The upper critical fields H_{c2} (T=0) scales with the Pauli limit as $H_{c2} \approx Hp = 1.84\ T_c$. We found that the upper critical field anisotropy for films thinner than 20 nm is dominated by dimensional effects. In addition, for films with thickness of 10 nm and 15 nm, λ(0) ≈ (800 ± 50) nm and H_c (0) = (500 ± 80) Oe values were estimated from the J_c ($T\to T_c$) for the 2D limit according with the GL predictions.

Acknowledgments

This work was partially supported by the ANPCYT (PICT 2015-2171) and CONICET PIP 2015-0100575CO. N H, SB and JG are members of the Instituto de Nanociencia y Nanotecnología, CNEA.

Table 1. Upper critical fields and related superconducting parameters for the different γ-Mo_2N.

Figure 1. *a)* AFM image of a 5 nm thick γ-Mo_2N grown at room temperature on 8 nm AlN / Si (001). *b)* AFM profile of the region indicated in *a)*.

Figure 2. *a)* XRD pattern diffractogram of a 260 nm thick γ-Mo_2N thin film. The step like discontinuity in the base line at ~65 degrees signals the absorption edge of the Ni filter used to discard the Cu K_β radiation, in this case of the (400) Si substrate peak. *b-d)* (200), (111) and (220) pole figures, respectively.

Figure 3. *a)* TEM cross-sectional image of a 40 nm thick γ-Mo_2N film grown on 8 nm thick AlN buffered Si (100). *b)* High resolution TEM image of the γ-Mo_2N film. Inset: The inset to the Fast Fourier transformation. Spots corresponding to the 111 reflexions are identified. *c)* Fourier filtered image of image *b)* using the 111 spots.

Figure 4. Long XPS spectrum (*a*) and Mo 3d spectra of the γ-Mo_2N pristine surface (*b*) and of the surface cleaned with Ar+ (2kV) (c). In vertical lines are indicated the references for Mo_2N at BE=228.6eV, for MoO_2 at BE=230eV and for MoO_3 at BE=232.7eV.

Figure 5. Thickness dependence of the superconducting critical temperature T_c in γ-Mo_2N film grown on 8 nm thick AlN buffered Si (100). Inset: Temperature dependence of the resisitivity at temperatures smaller than 10 K in the studied films. The criteria for the determination of T_c is indicated with dashed lines in the curve corresponding to a 5 nm thick Mo_2N thin film (*d5*).

Figure 6. Reduced temperature ($t = T / T_c$) dependence of the upper critical field (H_{c2}) with **H** parallel ($H_{c2}^{\parallel}$) and perpendicular ($H_{c2}^{\perp}$) to the surface for samples *a) d*5; *b) d*10; *c) d*15; *d) d*40.

Figure 7. *a)* Angular dependence of the critical current densities at 3.2 K and 3.65 K for *d*10 and *d*15 respectively. Both measurements were performed with 0.01 T. *b)* Normalized depairing current versus temperature. The dotted line corresponds to the GL prediction.

[1] Zhen Wang, Hirotaka Terai, Akira Kawakami, Yoshinori Uzawa, Interface and tunneling barrier heights of NbN/AlN/NbN tunnel junctions, Appl. Phys. Lett. 75 (1999) 701-703.
[2] M. Shcherbatenko, I. Tretyakov, Yu. Lobanov, S. N. Maslennikov, N. Kaurova, M. Finkel, B. Voronov, G. Goltsman, T. M. Klapwijk, Nonequilibrium interpretation of DC properties of NbN superconducting hot electron bolometers, Appl. Phys. Lett **109** (2016) 132602- 132605.
[3] Chandra M. Natarajan, Michael G. Tanner, Robert H. Hadfield, Superconducting nanowire single-photon detectors: physics and applications, Supercond. Sci. Technol. **25** (2012) 063001- 0630016.
[4] B. T. Matthias, J. K. Hulm, A Search for New Superconducting Compounds, Phys. Rev. **87** (1952) 799-806.
[5] Kei Inumaru, Kazuya Baba, Shoji Yamanaka, Synthesis and Characterization of Superconducting β-Mo_2N Crystalline Phase on a Si Substrate: An Application of Pulsed Laser Deposition to Nitride Chemistry, Chem. Mater. **17** (2005) 5935–5940.
[6] Kei Inumaru, Takanori Nishikawa, Kazuharu Nakamura Shoji Yamanaka, High-Pressure Synthesis of Superconducting Molybdenum Nitride δ-MoN by in Situ Nitridation, Chem. Mater. **20** (2008) 4756–4761.
[7] Shanmin Wang, Daniel Antonio, Xiaohui Yu, Jianzhong Zhang, Andrew L. Cornelius, Duanwei He, Yusheng Zhao, The Hardest Superconducting Metal Nitride, Scient. Rep 5 (2015) 13733 -13741.
[8] Tetsuya Kawashima, Eiji Takayama-Muromachi, Paul F. McMillan, High-pressure synthesis and crystal structure of γ-Mo2N, Phys. C **460-462** (2007) 651-652.
[9] V. Palmieri, New materials for superconducting radiofrequency cavities, The 10th Workshop on RF Superconductivity, Tsukuba, Japan, 2001, pp. 162-169.
[10] H. Ihara, M. Hirabayashi, K. Senzaki, Y. Kimura, H. Kezuka, Superconductivity of B1-MoN films annealed under high pressure, Phys. Rev. B **32** (1985) 1816-1817.
[11] Kei Inumaru, Kazuya Baba and Shoji Yamanaka, Structural distortion and suppression of superconductivity in stoichiometric B1−MoN epitaxial thin films Phys. Rev. B **73 (**2006) 52504-52507.
[12] D. K. Christen, S. T. Sekula, J. T. Ellis, J. D. Lewis, J. M. Williams, Formation, properties, and ion irradiation effects of hexagonal structure MoN thin films, IEEE Transactions on Magnetics **23** (1987) 1014-1018.
[13] Y. Y. Zhang, N. F. Haberkorn, F. Ronning, H. Wang, N. A. Mara, M. Zhuo, C. Li, J. H. Lee, K. J. Blackmore, E. Bauer, A. K. Burrell, T. M. Mccleskey, M. E. Hawley, R. K. Schulze, L. Civale, T. Tajima, Q. X. Jia, Epitaxial Superconducting δ-MoN Films Grown by a Chemical Solution Method, J. Am. Chem. Soc. **133** (2011) 20735 - 20737.
[14] Hongmei Luo, Guifu Zou, Haiyan Wang, Joon Hwan Lee, Yuan Lin, Huisheng Peng, Qianglu Lin, Shuguang Deng, Eve Bauer, T. Mark McCleskey, Anthony K. Burrell, Quanxi Jia,, Controlling Crystal Structure and Oxidation State in Molybdenum Nitrides through Epitaxial Stabilization, J. Phys. Chem. C **115** (2011) 17880–17883.
[15] M. Tinkham, Introduction to Superconductivity, 2nd edn, McGraw-Hill, 1996.
[16] S. Thakoor, J. L. Lamb, A. P. Thakoor, S. K. Khanna, High T_c superconducting NbN films deposited at room temperature, J. Appl. Phys. **58** (1985) 4643-4648.
[17] Zhen Wang, Akira Kawakami, Yoshinori Uzawa, Bokuji Komiyama, Superconducting properties and crystal structures of single-crystal niobium nitride thin films deposited at ambient substrate temperature, J. Appl. Phys. **79** (1996) 7837-7842.
[18] A. Gurevich, Enhancement of rf breakdown field of superconductors by multilayer coating, Appl. Phys. Lett. **88** (2006) 012511-012513.
[19]A. Verevkin, J. Zhang, Roman Sobolewski A. Lipatov, O. Okunev, G. Chulkova, A. Korneev, K. Smirnov, G. N. Gol'tsman, A. Semenov, Detection efficiency of large-active-area NbN single-photon superconducting detectors in the ultraviolet to near-infrared range, Appl. Phys. Lett. **80** (2002) 4687-4689.
[20] R. Baskaran, A. V. Thanikai Arasu, E. P. Amaladass, L. S. Vaidhyanathan, D. K. Baisnab Increased upper critical field for nanocrystalline MoN thin films deposited on AlN buffered substrates at ambient temperature, J. Phys. D **49** (2016) 205304-205307.

[21] M. Morita, M. Morita, T. Ohmi, E Hasegawa, M. Kawakami, and M. Ohwada, Growth of native oxide on a silicon surface, **68** (1990) 1272 - 1281.
[22] Zhen Wang, Hirotaka Terai, Akira Kawakami, and Yoshinori Uzawa, Interface and tunneling barrier heights of NbN/AlN/NbN tunnel junctions, Appl. Phys. Lett. 75 (1999) 701-703.
[23] C. Braun, Parratt32 or the reflectometry tool, HMI, Berlin, 1997–1999, http://www.helmholtz-berlin.de.
[24] Geug-Tae Kim, Tae-Keun Park, Hongsuk Chung, Young-Tae Kim, Moo-Hyun Kwon, Jeong-Gil Choi, Growth and characterization of chloronitroaniline crystals for optical parametric oscillators: I. XPS study of Mo-based compounds, Appl. Surf Scie **152** (1999) 35-43.
[25] Z. B. Zhaobin Wei, P. Grange, B. Delmon, XPS and XRD studies of fresh and sulfided Mo_2N, Appl. Surf. Scie **135** (1998) 107–114.
[26] Y. M. Wang, R. Y. Lin, Amorphous molybdenum nitride thin films prepared by reactive sputter deposition, Mater. Sci. Eng. B **112** (2004) 42-49.
[27] Muneyoshi Yamada, Junichi Yasumaru, Marwan HouaUa, David M. Hercules, Distribution of Molybdenum Oxidation States in Reduced Mo/Al_2O_3 Catalysts. Correlation with Benzene Hydrogenation Activity, J. Phys. Chem. **95** (1991) 7037-7042.
[28] N. Haberkorn, S. Bengio, S. Suárez, P. D. Pérez, M. Sirena and J. Guimpel. Effect of the nitrogen-argon gas mixtures on the superconductivity properties of reactively sputtered molybdenum nitride thin films.arXiv:1708.05219.
[29] H. Luo, G. Zou, H. Wang, J. H. Lee, Y. Lin, H. Peng, Q. Lin, S. Deng, E. Bauer, T. M. McCleskey, A. K. Burrell, and Q. Jia, Controlling Crystal Structure and Oxidation State in Molybdenum Nitrides through Epitaxial Stabilization, J. Phys. Chem. C **115** (2011) 17880 – 17883.
[30] N. Haberkorn, Y. Y. Zhang, J. Kim, T. M. McCleskey, A. K. Burrell, R. F. Depaula, T. Tajima, Q. X. Jia, L. Civale, Upper critical magnetic field and vortex-free state in very thin epitaxial δ-MoN films grown by polymer-assisted deposition, Supercond. Sci. Technol. **26** (2013) 105023 – 105029.
[31] N. R. Werthamer, E. Helfand, P. C. Hohenberg, Temperature and Purity Dependence of the Superconducting Critical Field, Hc2. III. Electron Spin and Spin-Orbit Effects Phys. Rev. **147** (1966) 295-302.
[32] B. J. Yuan, J. P. Whitehead, Angular dependence of the upper critical field in superconducting films, Phys. C **231** (1994) 395-408.
[33] N. Takezawa, T. Koyama, M. Tachiki, Angular dependence of the upper critical field in layered superconductors, Phys. C **207 (**1993) 231-238.
[34] K. Maki, Effect of Pauli Paramagnetism on Magnetic Properties of High-Field Superconductors, Phys. Rev. **148** (1966) 362-369.
[35] A. M. Clogston, Upper limit for critical field in hard superconductors, Phys. Rev. Lett. 9 (1962) 266-267.
[36] L. Civale, B. Maiorov, A. Serquis, J. O. Willis, J. Y. Coulter,H. Wang, Q. X. Jia, P. N. Arendt, M. Jaime, J. L. MacManus-Driscoll, M. P. Maley,S. R. Foltyn, Understanding High Critical Currents in $YBa_2Cu_3O_7$ Thin Films and Coated Conductors, J. Low Temp. Phys. **135** (2004) 87-98.
[37] Shi-Zeng Lin, Oscar Ayala-Valenzuela, Ross D. McDonald, Lev N. Bulaevskii, Terry G. Holesinger, Filip Ronning, Nina R. Weisse-Bernstein, Todd L. Williamson, Alexander H. Mueller, Mark A. Hoffbauer, Michael W. Rabin, Matthias J. Graf, Characterization of the thin-film NbN superconductor for single-photon detection by transport measurements, Phys. Review B 87 (2013) 184507-184516.
[38] J. M. E. Geers, M. B. S. Hesselberth, J. Aarts, A. A. Golubov, Depairing currents in the superconductor/ferromagnet proximity system Nb/Fe, Phys. Rev. B **64** (2001) 94506-94513.
[39] A. Yu. Rusanov, M. B. S Hesselberth, J Aarts, Depairing currents in superconducting films of Nb and amorphous MoGe,Phys. Rev. B **70** (2004) 24510-24514.

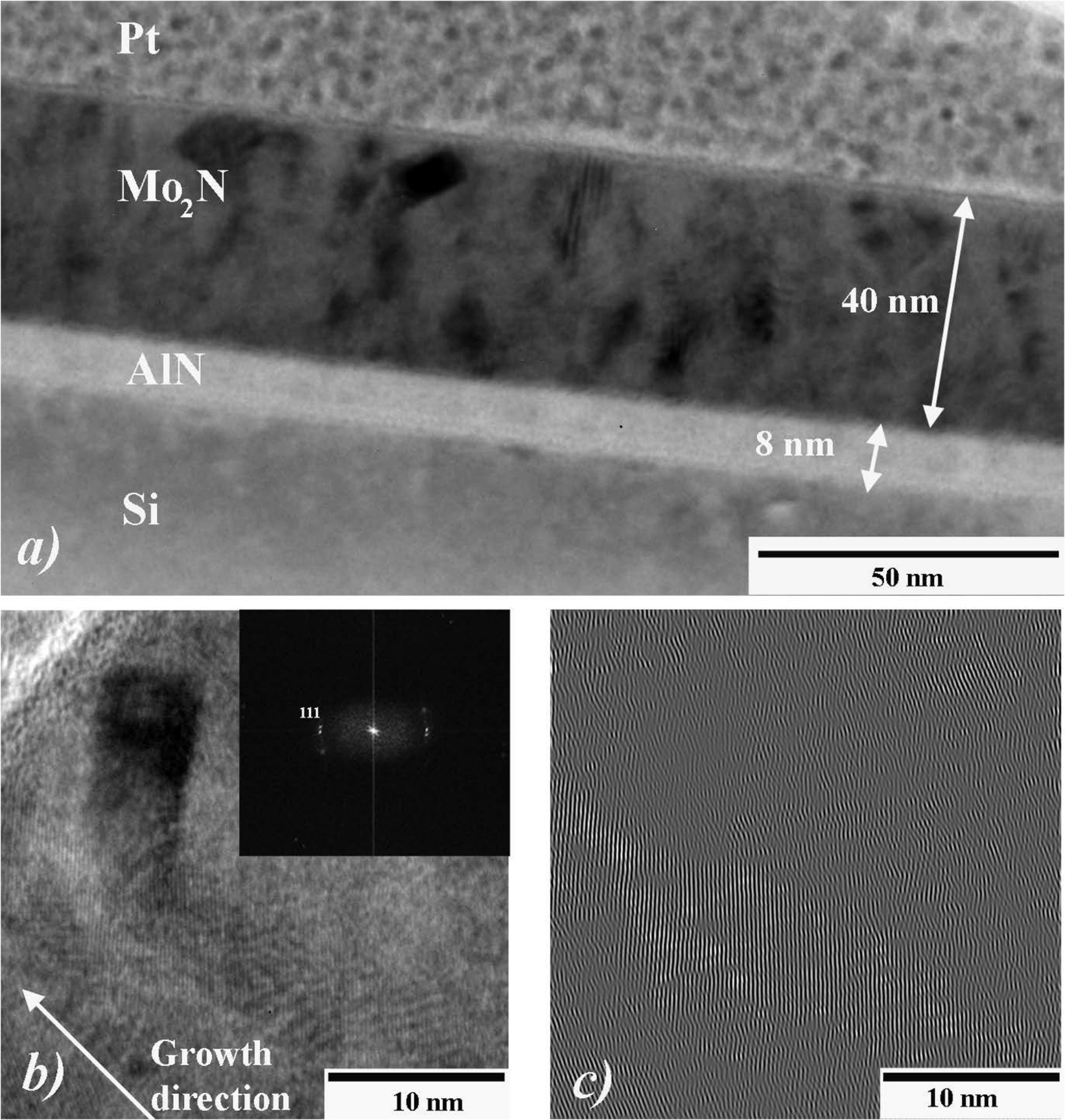
Pt
Mo_2N
AlN
Si
40 nm
8 nm
50 nm
a)
111
b)
Growth direction
10 nm
c)
10 nm

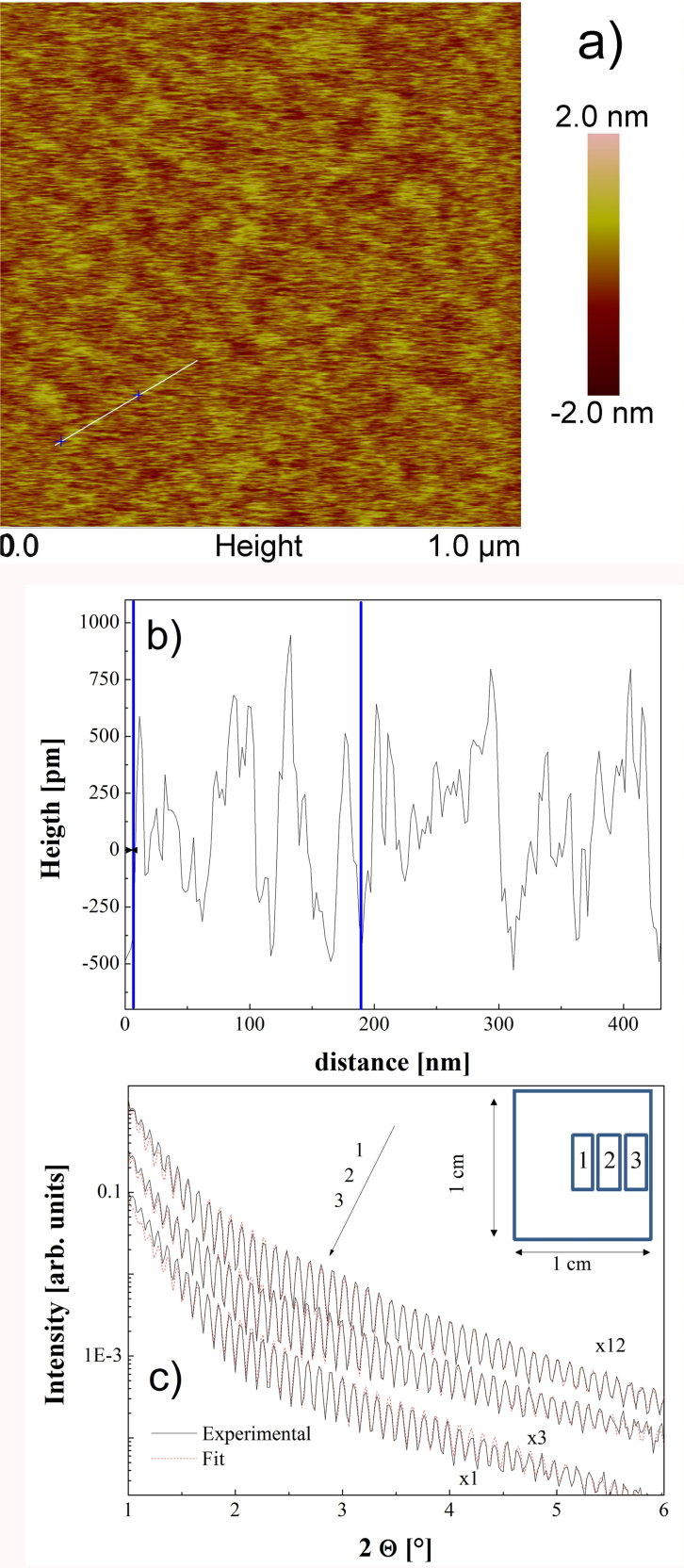
a)
2.0 nm
-2.0 nm
0.0
Height
1.0 µm
b)
Heigth [pm]
1000
750
500
250
0
-250
-500
0
100
200
300
400
distance [nm]
c)
Intensity [arb. units]
0.1
1E-3
1
2
3
1 cm
1 cm
1
2
3
x12
x3
x1
Experimental
Fit
1
2
3
4
5
6
2 Θ [°]

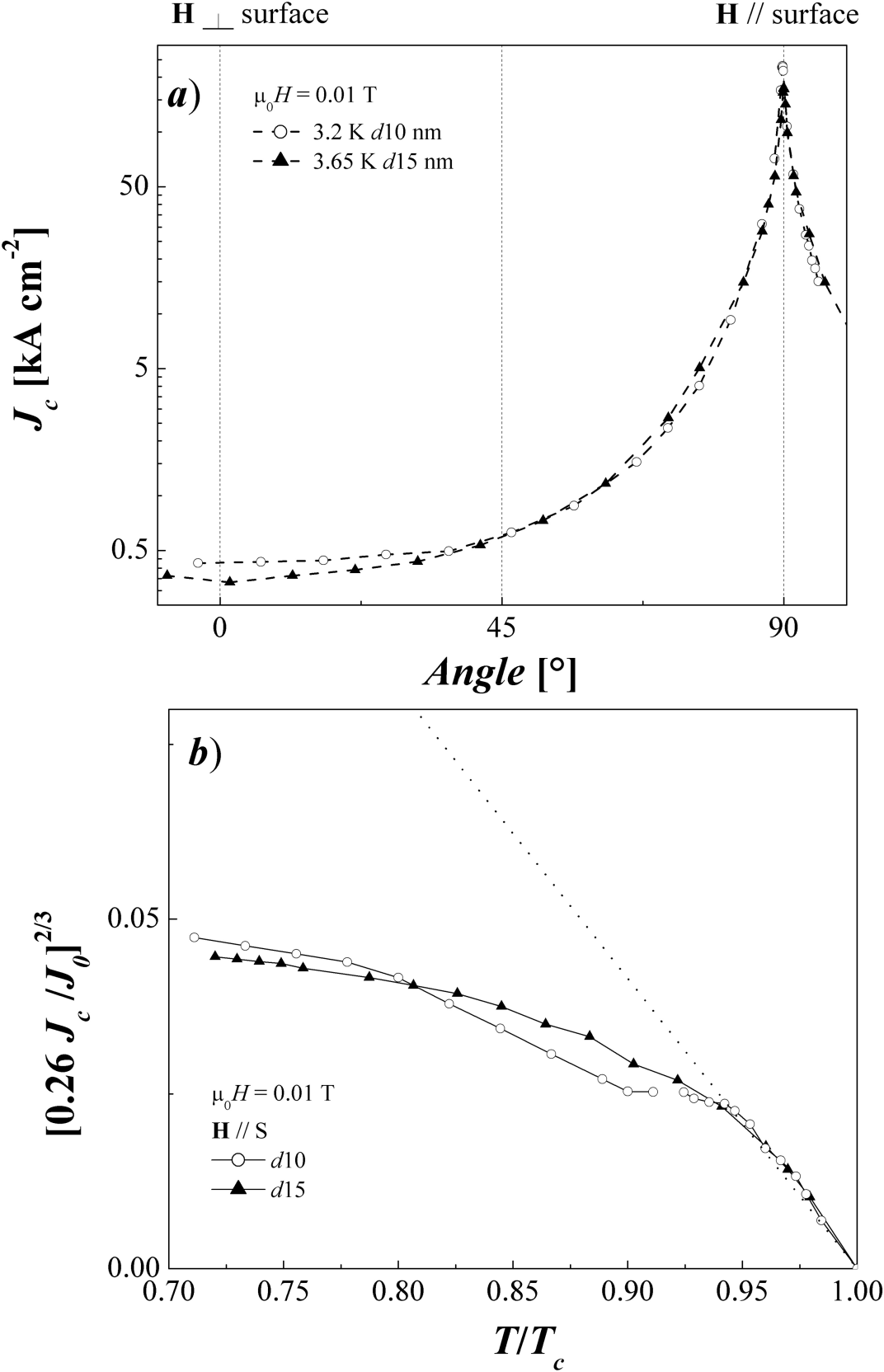
H ⊥ surface
H // surface
a)
μ0H = 0.01 T
3.2 K d10 nm
3.65 K d15 nm
Jc [kA cm-2]
50
5
0.5
0
45
90
Angle [°]
b)
[0.26 Jc /J0]2/3
0.05
0.00
μ0H = 0.01 T
H // S
d10
d15
0.70
0.75
0.80
0.85
0.90
0.95
1.00
T/Tc

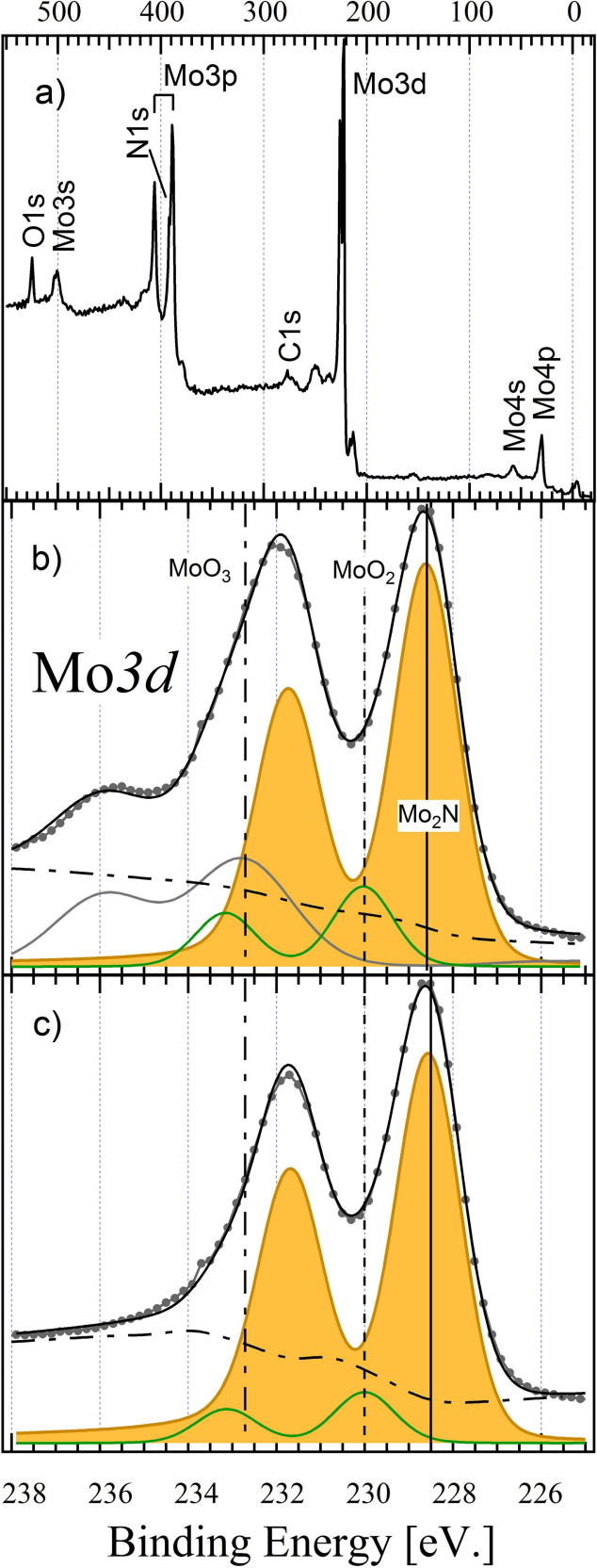
500
400
300
200
100
0
a)
Mo3p
Mo3d
N1s
O1s
Mo3s
C1s
Mo4s
Mo4p
b)
MoO3
MoO2
Mo3d
Mo2N
c)
238
236
234
232
230
228
226
Binding Energy [eV.]

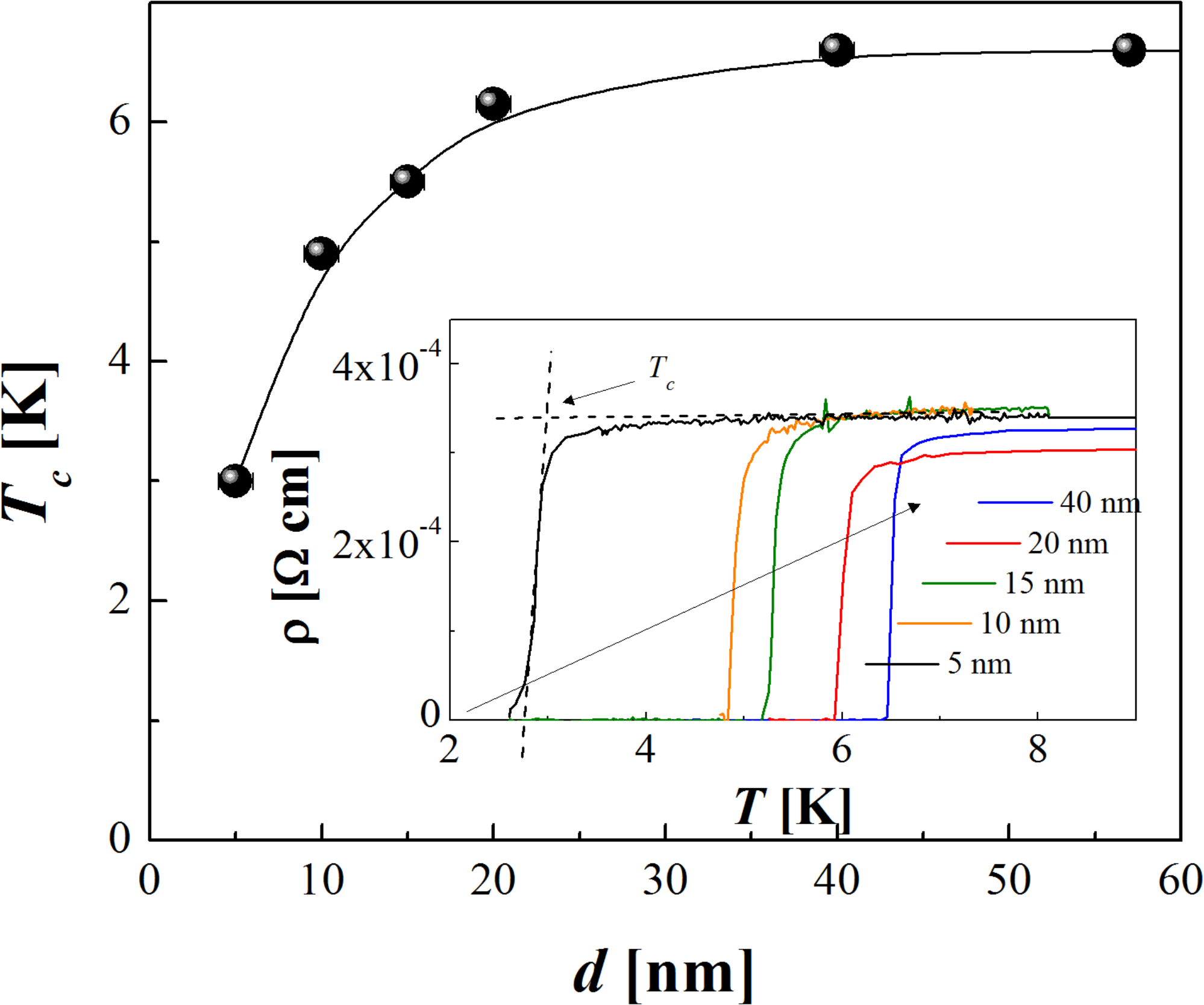
T_c [K]
d [nm]
0
2
4
6
0
10
20
30
40
50
60
ρ [Ω cm]
4x10^{-4}
2x10^{-4}
0
T_c
2
4
6
8
T [K]
40 nm
20 nm
15 nm
10 nm
5 nm

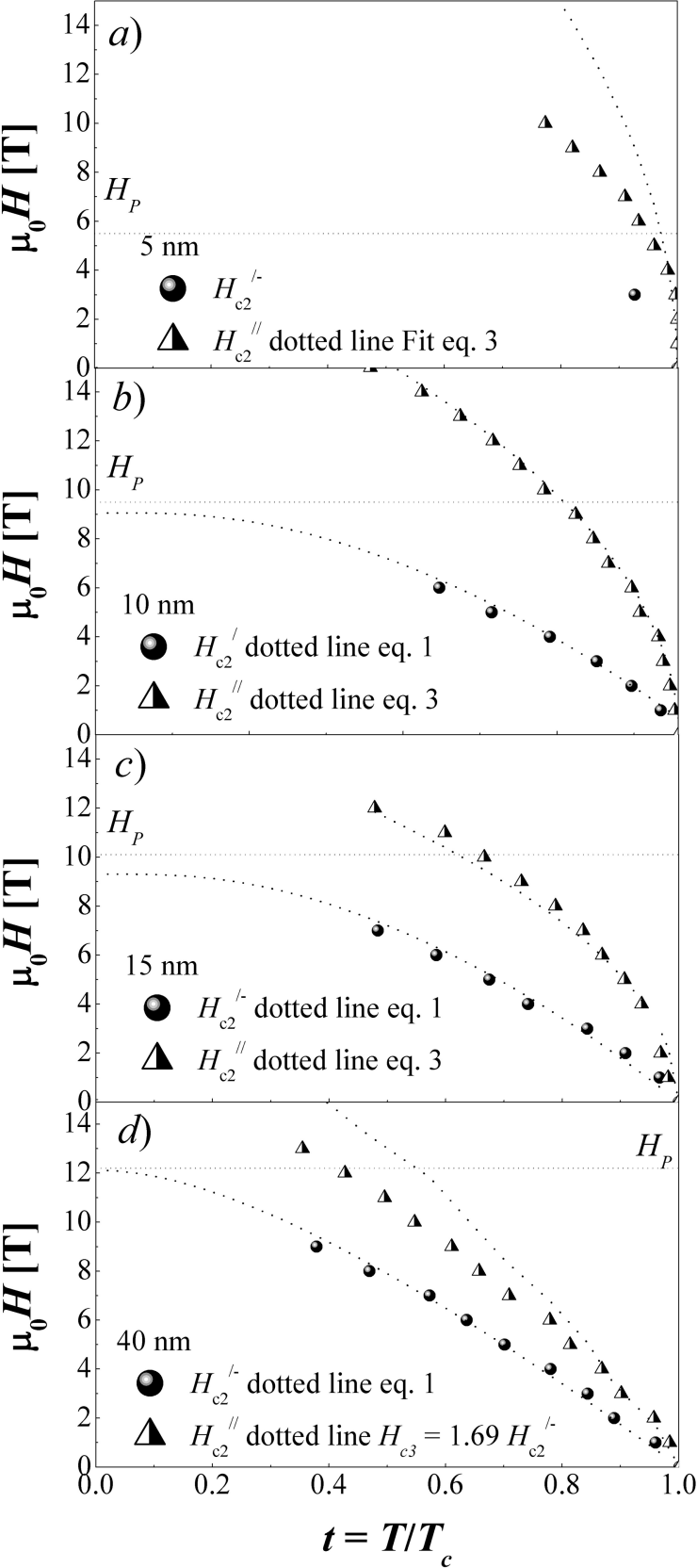
a)
H_P
5 nm
$H_{c2}^{/-}$
$H_{c2}^{//}$ dotted line Fit eq. 3
b)
H_P
10 nm
$H_{c2}^{/}$ dotted line eq. 1
$H_{c2}^{//}$ dotted line eq. 3
c)
H_P
15 nm
$H_{c2}^{/-}$ dotted line eq. 1
$H_{c2}^{//}$ dotted line eq. 3
d)
H_P
40 nm
$H_{c2}^{/-}$ dotted line eq. 1
$H_{c2}^{//}$ dotted line $H_{c3} = 1.69\ H_{c2}^{/-}$
$\mu_0 H$ [T]
$t = T/T_c$
0.0
0.2
0.4
0.6
0.8
1.0
0
2
4
6
8
10
12
14

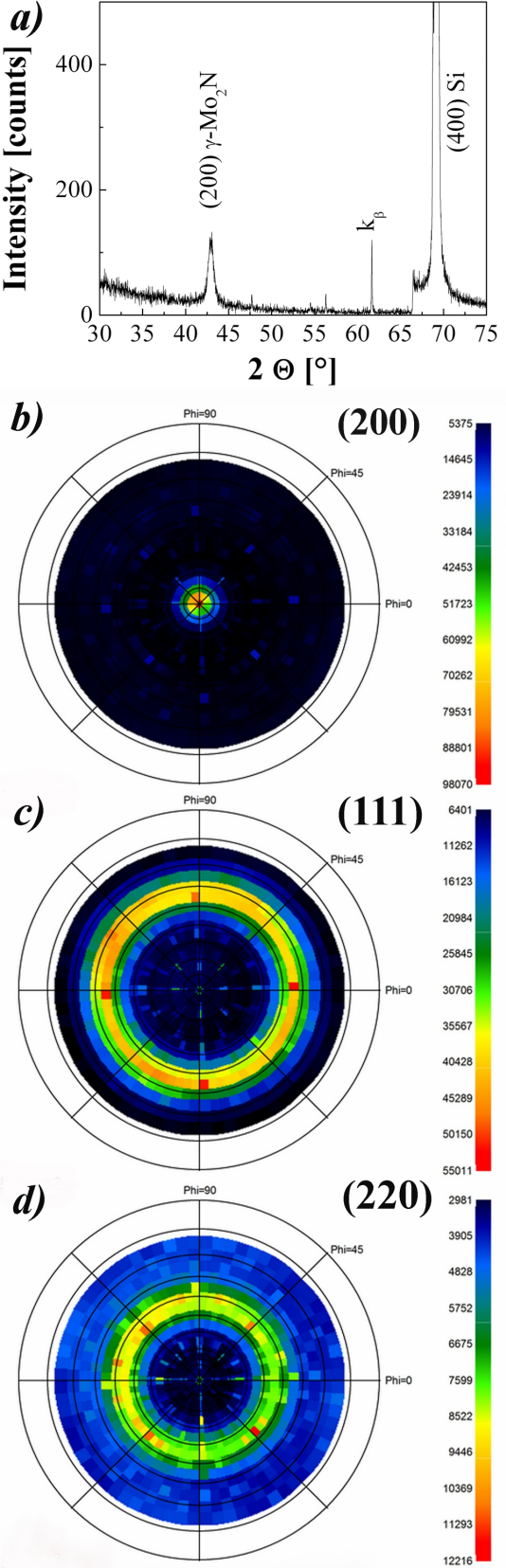
a)
Intensity [counts]
400
200
0
(200) γ-Mo2N
kβ
(400) Si
30 35 40 45 50 55 60 65 70 75
2 Θ [°]
b)
(200)
Phi=90
Phi=45
Phi=0
5375
14645
23914
33184
42453
51723
60992
70262
79531
88801
98070
c)
(111)
Phi=90
Phi=45
Phi=0
6401
11262
16123
20984
25845
30706
35567
40428
45289
50150
55011
d)
(220)
Phi=90
Phi=45
Phi=0
2981
3905
4828
5752
6675
7599
8522
9446
10369
11293
12216

Sample	Thickness [nm]	T_c [K]	RRR	ρ [Ω.cm]	$-\left[\frac{\delta H_{c2}}{\delta T}\right]_{T_c}$ [T/K]	α	$H_{c2}^{\perp}$ [T]	ξ (0) [nm]
*d*5	5	3	0.92	$3.2\text{x}10^{-4}$	--	-	-	
*d*10	10	4.9	0.9	$3.1\text{x}10^{-4}$	4	0.8-1	9.0 (0.1)	6.0
*d*15	15	5.5	0.9	$3.0\text{x}10^{-4}$	3.8	0.8-1	9.3 (0.1)	5.9
*d*20	20	6.6	0.93	$2.8\text{x}10^{-4}$	-	-	-	
*d*40	40	6.6	0.93	$3.2\text{ x}10^{-4}$	2.65	0	12.0 (0.2)	5.2